Construction of a Predictive Model for Assessing the Porosity of TiNi Materials Based on Sintering Parameters of Samples

Viktor V. Nikolaev[1], Tatiana B. Lepekhina[1], Georgii V. Malkin[1], Natalya A. Krivova[1], Denis A. Grigoriev[1], Alexander S. Garin[1], Ekaterina S. Marchenko[1,2], Maxim D. Khomenko[3], and Yury V. Kistenev[1*]

[1] Tomsk State University, 36 Lenin Ave., Tomsk 634050, Russian Federation
[2] Institute for Problems of Chemical and Energetic Technologies of the Siberian Branch of RAS, 1 Sotsialisticheskaja str., Biysk 659332, Russian Federation
[3] NRC "Kurchatov Institute", 1 Kurchatov Sq., Moscow 123182, Russian Federation
*e-mail: yuk@iao.ru

Abstract. Additive manufacturing of TiNi alloys has developed significantly in recent years. Such growth is due to the unique properties of the resulting designs – superelasticity, bending strength – stretching, corrosion, chemical and thermodynamic stability. In addition, three-dimensional (3D) printing technology significantly expanded the scope of use of this material in various applied areas from biomedicine (for printing implants and bone tissue engineering), to, for example, the automotive and aerospace industries. Despite the fact that 3D printing technology already has commercial solutions that allows producing complex-shaped structures, this area is in the stage of development. Of a particular interest is the optimization of printing process and the development of a quality control system (achieving the required parameters of porosity, roughness, minimizing defects such as cracks, contamination, delamination, surface and subsurface heterogeneities, surface quality, shrinkage, etc.). In this paper, an original non-destructive method for assessing the sintering temperature as an indirect measure of porosity of a material using optical coherence tomography (OCT) and machine learning methods is proposed. Random Forest Regression approach was used to predict depth maps and spatial statistics from the sintering temperature. The Random Forest model based on the first- and the second-order texture metrics of OCT images provided R^2 of about 0.95 for sintering temperature prediction.

Keywords: TiNi; porosity; biocompatibility; optical coherence tomography; machine learning.

Paper #9280 received 13 Jun 2025; revised manuscript received 3 Aug 2025; accepted for publication 21 Aug 2025; published online 28 Sep 2025. doi: 10.18287/JBPE25.11.030305.

1 Introduction

Alloys based on the intermetallic nickel-titanium compound (TiNi) have gained widespread use due to their unique combination of physical and mechanical properties, which allow successful resolution of various technical and medical challenges [1]. Shape memory effect, superelasticity, high corrosion resistance and biocompatibility make these materials highly attractive for creating devices and structures with enhanced or fundamentally new functionalities [2, 3]. Current technologies allow producing both monolithic and porous structures based on TiNi, each possessing its own set of functional and mechanical characteristics [4]. Porous TiNi alloys are of particular interest due to their extensive use in medicine, facilitated by their hysteresis properties similar to human biological tissues and their developed three-dimensional porous structure morphologically akin to bone tissue. Such characteristics contribute to effective biological integration of implants [1]. Powder metallurgy methods have produced porous TiNi-based products applied in various medical fields, including oncology, dentistry and maxillofacial surgery [5, 6].

In calcium-hydride reduction method of TiNi-based powder production [7], initial titanium and nickel compounds are reduced by calcium (most commonly in the presence of calcium hydride), resulting in the formation of TiNi intermetallic powder. TiNi powder produced by this method typically exhibits a complex phase composition: in addition to the main TiNi phase (present in two structural states – high-temperature B_2 phase and martensitic B19'), secondary intermetallic phases enriched with titanium (Ti_2Ni) and nickel ($TiNi_3$) are detected, along with metastable phases such as Ti_3Ni_4 and oxide inclusions like Ti_4Ni_2 (O,N,C – oxycarbonitride).

The initial powders define the structural parameters and physical-mechanical properties of porous materials obtained by powder metallurgy techniques. The diffusion sintering method of ready-made TiNi powder allows producing material with a more homogeneous phase-chemical composition compared to materials synthesized by self-propagating high-temperature synthesis (SHS) or reactive sintering using titanium and nickel powders [8, 9]. A general tendency in sintering is a decrease in overall porosity with increased sintering conditions. Elevated sintering temperature enhances particle diffusion bonding (growth of "necks" between particles), leading to pore shrinkage and thus reducing the total porosity of the material [10]. Simultaneously, pore enlargement may occur as smaller pores partially merge into larger ones, as observed by the authors of study [11], where increasing sintering temperature from 950 °C to 1000 °C raised the average pore size from approximately 36 to 182 μm.

Reducing the size of the initial powder particles promotes more intense sintering and increased material density – a finer powder yields lower residual porosity compared to coarser powder under otherwise equal conditions [10]. Isothermal holding time has a similar effect: extending sintering time usually enhances the degree of sintering and reduces porosity due to further growth of contacts between particles. For example, a decrease in porosity from ~41% to ~39% when holding time increased from 2 to 6 min was shown [12].

TiNi-based alloys are extremely sensitive to melting temperature regimes: even slight variations in melting point or heating/cooling rates can profoundly influence the microstructure of the porous alloy, its physic-mechanical properties, and characteristics of martensitic transformations [1]. Therefore, control of thermal parameters during sintering – especially the exact maintenance of melting temperatures – determines the properties of porous TiNi-based materials.

Porosity is one of the key factors affecting the biocompatibility of materials with body tissues. Biocompatibility is the ability of a material to integrate with the patient's tissues without causing any adverse clinical reactions [13]. In addition, this applies to the stimulation of cellular and tissue reactions to achieve engraftment. Important biocompatibility characteristics ensuring the engraftment of implants are the absence of inflammation, necrosis and severe oxidative stress in the implantation area [14]. Biocompatibility is largely determined by the surface structure of the implant. Biocompatible materials should not cause pathological processes or enhance complications, should not have a carcinogenic effect on the body [15]. Porosity affects cell survival, providing space for their attachment and migration [5, 16]. The optimal pore size, which forms a rough surface of the biomaterial, has a positive effect on morphology and proliferation [17, 18]. It is widely recognized that pore size and porosity affect significantly the progression of osteogenesis [19]. The interconnected pore network provides sufficient permeability for the exchange of nutrients and metabolic waste between cells and the extracellular matrix (ECM). This promotes the osteogenesis process, including cell colonization, differentiation and ECM deposition [20].

When fabricating implants intended to replace lost bone areas or entire bone, it is necessary to consider the mechanical properties of biomaterials, which should match the mechanical properties of bone. Such implants should have high corrosion resistance to prevent implant wear. In Ref. [21], Ti scaffolds were fabricated in two porosity ranges (50% and 70%), so their mechanical properties could mimic those of cortical and trabecular bone. It was concluded that scaffolds with a pore size range of 45 to 106 μm have the best micro-architecture suitable for early stages of cell attachment. 3D titanium scaffolds with a pore size of 600 to 700 μm and a porosity of 70% to 90% was found to demonstrate favorable prospects for osteogenesis and restoration of bone defects [22].

The fundamental characteristic of porosity is the relative pore area. Some authors determine the pore volume, or construct a pore size distribution. For example, for an optical microscope, the pore area can be estimated relative to the total area of the sample. However, this characteristic does not take into account the pore depth distribution, and an approximate determination of the focus at the same point of different samples can affect the final result.

Various data processing methods are used for porosity analysis. A new model for predicting the porosity of TiNi alloy based on the Support Vector Machine (SVM) was proposed [23]. Gaussian process regression [24], multiple linear regression, random forest [25], and convolutional neural network [26] were used to predict porosity in material manufacturing. In a previous study [27], we used optical coherence tomography (OCT) to investigate the porosity of TiNi samples. Porosity is a fundamental property of the material that manifests as texture in an OCT scan, whereas sintering temperature is a process parameter that is not directly visualized. OCT was proven to be an alternative technique for evaluating the porosity of TiNi biomaterials. Researchers trained the SVM with a radial basis function kernel classifier based on the first- and the second-order statistics of OCT data to distinguish groups of TiNi samples. The classifier provided an accuracy of $95 \pm 5\%$ for two groups of TiNi samples classification. This work demonstrated the effectiveness of machine learning (ML) methods for analysis the porosity of TiNi biomaterials, and it can be used to analyze the porosity of other biomedical materials as well. The combination of OCT and ML has been little studied and is not practically presented in the literature. Therefore, this study is relevant and promising.

Thus, the purpose of this work is to develop a predictive model for assessing the porosity of TiNi based on different sintering temperatures of the samples.

2 Materials and Methods

2.1 TiNi Preparation

Production of porous TiNi samples was carried out using diffusion liquid-phase sintering of TiNi powder grade PV–N55T45 (Fig. 1, Table 1), previously obtained by the calcium-hydride reduction method. Before sintering, the powder was dried in a laboratory vacuum oven at a temperature of 150–170 °C and residual pressure of 10^{-4} Pa for 4 h to remove adsorbed gases and moisture. The powder was then loaded without pressing into quartz tubes of 15 mm a diameter and a length of 100 mm, ensuring an initial bulk porosity of approximately 70%, necessary to achieve the optimal structure of the porous material.

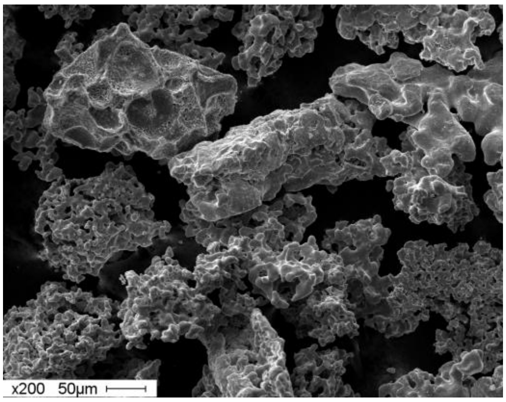

Fig. 1 Micrograph of powders: TiNi powder grade PV–N55T45.

The ends of the quartz tubes filled with powder were sealed with porous TiNi plugs produced by SHS. Subsequently, the tubes were placed into the working chamber of an electric vacuum furnace SNVE–1.31/16–I4 (Fig. 2).

Diffusion liquid-phase sintering was conducted at the following temperatures: 1230, 1240, 1250, 1260 and 1270 °C. Throughout the entire sintering process, the working chamber maintained a pressure of about $6.65 \cdot 10^{-4}$ Pa and the average heating rate of the samples was 10 °C/min. Upon reaching the target temperature, the samples were held isothermally for 15 min, after which heating was stopped, and the furnace was cooled to room temperature over 3 h. The sintered samples were then removed from the working chamber and extracted from the quartz tubes for further analysis.

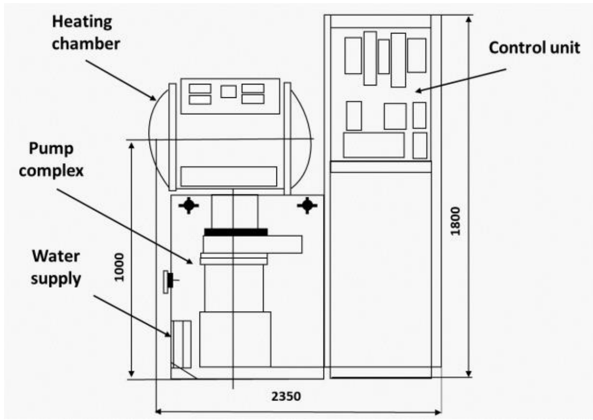

Fig. 2 Schematic diagram of the SNVE-1.31/16-I4 vacuum furnace.

2.2 OCT Protocol

The measurements were conducted using optical coherence tomograph GANIMEDE-II (Thorlabs, USA), which includes a basic scanning module OCTG-900 and super-luminescent diode with an operating wavelength of 930 ± 50 nm.

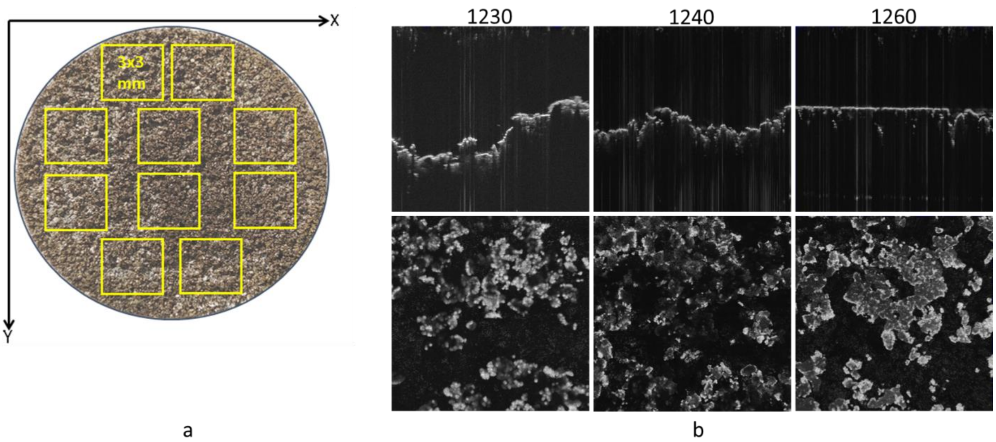

Fig. 3 (a) Schematic demonstration of disjoint scanning areas on the TiNi surface with size 3×3 mm, (b) examples B-scans (top) and C-scans (bottom) for test samples.

On the surface of the investigated sample TiNi, 3×3 mm area was highlighted using software ThorImageOCT 5.0.1, which was scanned with penetration depth up to 2.9 mm and the voxel size of 6×6×2.9 μm (the last parameter is the depth, *Z*-coordinate). Then the scan area was moved 10 times in parallel along the horizontal plane *XY* (Fig. 3(a)).

The scanning procedure was repeated on the lower edge of the sample. For a group of 5 samples sintered at different temperatures, 100 regions were scanned for all groups (in total, 500 regions). Examples of source data of images are shown in Fig. 3(b).

2.3 Data Preprocessing

For the analysis of TiNi sample's surfaces, a depth map method was applied. For every OCT A-scan from investigated area, *Z*-coordinate of its intensity maximum was determined, which corresponds to the boundary between air and metal at a point on a sample surface (Fig. 4).

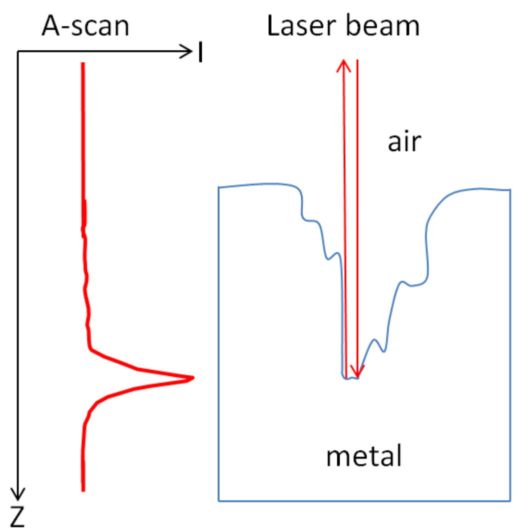

Fig. 4 Schematic representation of an OCT A-scan for TiNi sample and its intensity maximum, which corresponds to the boundary between air and metal.

For the *Z*-coordinates of the intensity maximum, their distribution was constructed and a 5-percentile value was calculated in the initial area corresponding to the boundary of the sample surface. Then, the maximal pore depth for all groups of samples was found, which was 1470 μm. Considering this, the depth map, which is a 3D surface, where *XY*-coordinates corresponded to A-scan positions on the area, *Z*-coordinate − pore depth at a given point, was constructed. To reduce the noise, median and Gaussian filters were applied to the depth map.

2.4 Statistical Analysis and Data Processing

The porosity (%) of a depth slice can be calculated as follows:

$$Porosity = 100 * \frac{S_P}{S_T}, \quad (1)$$

where S_P – the total pore area, S_T – the total slice area. For the quantitative description of the depth map, the first- and the second-order statistics were calculated. The following distinctive characteristics of the first-order statistics were used:

$$\text{Mean: } \nu = 2.94 * \sum_{i=0}^{k-1} i * p_i, \quad (2)$$

$$\text{STD: } \sigma = 2.94 * \sqrt{\sum_{i=0}^{k-1} p_i * (i-\nu)^2}, \quad (3)$$

$$\text{Shannon entropy: } H = -\sum_{i=0}^{k-1} (p_i * \log(p_i)), \quad (4)$$

$$\text{Kurtosis: } \gamma_2 = \frac{\mu_4}{\sigma^4} - 3, \quad (5)$$

$$\text{Skew: } A_s = \frac{\mu_3}{\sigma^3}, \quad (6)$$

where ν – the first raw moment of the mean values of pore depth in the studied area, k – the number of values for a single depth map element, p_i – the probability of depth's value equal to $i * 2.94$ μm (i is the number of step along *Z*-coordinate grid), σ – the standard deviation (STD) from the mean value ν, μ_3 – the third central moment, μ_4 – the fourth central moment. The *n*-th order raw moment is following:

$$\nu_n = E[X^n], \quad (7)$$

the *n*-th order central moment is:

$$\mu_n = E[(X - E[X])^n], \quad (8)$$

where E – the mathematical expectation, X – the random value.

The gray-level co-occurrence matrix (GLCM) for every depth map was built to calculate the second order statistics. The GLCM is following:

$$P_{i,j} \equiv P_{\triangle x, \triangle y}(i,j) = \sum_{x=1}^{n} \sum_{y=1}^{m} \begin{cases} 1, & if\ I(x,y)=i\ and\ I(x+\triangle x, y+\triangle y)=j \\ 0, & otherwise \end{cases}, \quad (9)$$

where P – GLCM with size (k,k), $(\Delta x, \Delta y)$ – offset from the considered pixel, when GLCM constructing, $I(x,y)$ – the value of the *Z*-coordinates corresponding to the boundary between air and metal.

For the second-order statistics, the following parameters were considered:

$$\text{Correlation: } \rho = \sum_{i,j=0}^{k-1} P_{i,j} * \left[\frac{(i-\nu_i)(j-\nu_j)}{\sqrt{\sigma_i^2 \sigma_j^2}}\right], \quad (10)$$

$$\text{Entropy: } H = \sum_{i,j=0}^{k-1} -P_{i,j} * \log(P_{i,j}), \quad (11)$$

$$\text{Contrast: } k = \sum_{i,j=0}^{k-1} P_{i,j} * (i-j)^2, \quad (12)$$

$$\text{Dissimilarity: } D = \sum_{i,j=0}^{k-1} P_{i,j} * |i-j|, \quad (13)$$

Homogeneity: $Q = \sum_{i,j=0}^{k-1} \frac{P_{i,j}}{1+(i-j)^2}$, (14)

Angular Second Moment (ASM): $A = \sum_{i,j=0}^{k-1} P_{i,j}^2$, (15)

Energy: $E = \sqrt{ASM}$, (16)

where $P_{i,j}$ – elements of the GLCM, ν_i and ν_j – mean values of the GLCM elements along i-line and j-row, respectively.

The statistical significance of differences was analyzed using the nonparametric Mann-Whitney test.

3 Results

The examples of photographs from 5 different groups (for 5 different temperatures) of TiNi samples are shown in Fig. 5(a). Each sample was studied according to the OCT protocol presented in the Materials and Methods section. There are two variants of processing C-scans in this analysis. The first one is based on manual selection surface depth. After that, area near surface was used and 95% quantiles were calculated [27] (see examples in Fig. 5(b)). The second one is based on 2D depth map calculation (the examples are shown in Fig. 5(c)).

Demonstration of the porosity distribution by depth constructed for each sample group, using the algorithm described in the Materials and Methods section, is shown in Fig. 6. At depths larger than 800 μm, the porosity is insignificant.

The cumulative sum for this function is the volume of pores, which do not fall within the optical shadow region. The first and the second-order statistics were presented in Fig. 7 and Fig. 8.

The TiNi samples produced at 1230 °C and 1240 °C have less pronounced changes compared to those of 1260 °C and 1270 °C (Fig. 7).

Correlation analysis revealed the relationship between the texture features of OCT images and their potential role in porosity assessment (Fig. 9). A strong negative correlation is observed between homogeneity and GLCM entropy ($r = -0.97$) having the obvious meaning: more homogeneous materials have less texture variability. Contrast and dissimilarity features form a cluster with high mutual correlation ($r > 0.95$) and are negatively related to the entropy ($r \approx -0.75$), confirming their sensitivity to pore boundaries. Energy, ASM parameters demonstrate an almost linear dependence ($r = 0.94$), which indicates the admissibility of excluding duplicate features when building models. Interestingly, GLCM correlation is weakly related to other metrics ($|r| < 0.33$), indicating its unique contribution to the description of textural features. The revealed dependencies are consistent with theoretical expectations: an increase in porosity leads to an increase in contrast and entropy with a decrease in homogeneity, which confirms the adequacy of the selected features for non-destructive testing.

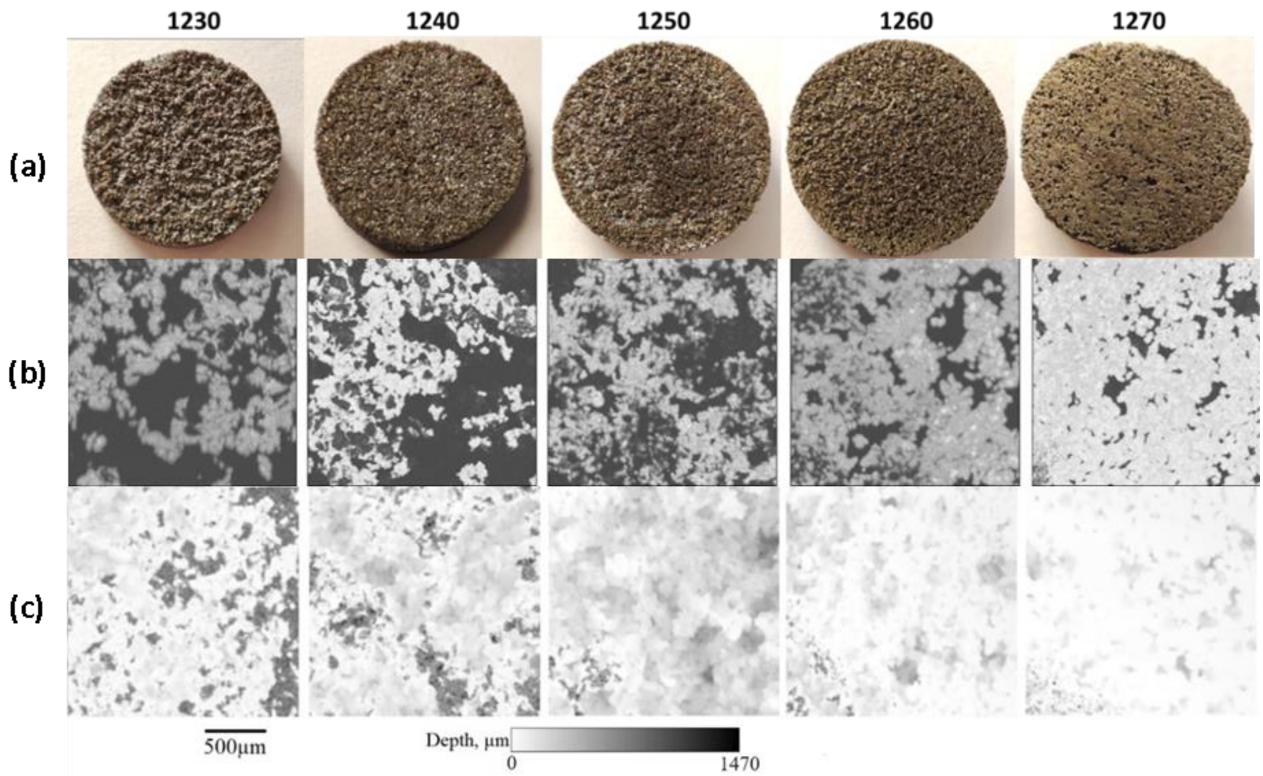

Fig. 5 (a) Photos of the TiNi samples at different temperatures, (b) normalized section of the samples surface, (c) corresponding depth maps.

 doi: 10.18287/JBPE25.11.030305

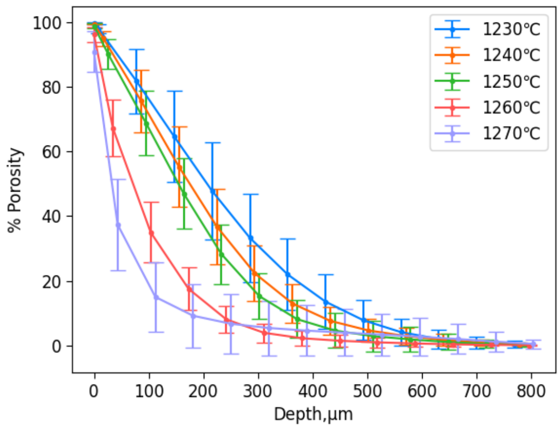

Fig. 6 Dependence of pore area on the depth.

The TiNi sample production temperature values were used to predict the final material properties. The prediction was made based on the first and the second-order statistics calculated for the OCT depth map. Random Forest Regressor (RFR) was selected due to its inherent advantages for our dataset: the relationship between OCT features (e.g., texture metrics, speckle contrast) and porosity is often non-linear, which RFR captures effectively through decision trees. In RFR, the ensemble approach with bootstrapping reduces variance and helps prevent overfitting, critical for our limited sample dataset size. Also, RFR provides native feature importance scores. The training set consisted of 400 depth maps, 80 images from each class. The data were split into training and testing sets in the ratio of 80%/20%. Then, the prediction models were tested using the *K*-fold cross-validation approach. This procedure was repeated 5 times, so that each part of the data from one sample was included in the test set only once. The RFR prediction accuracy is presented in Table 1. The feature vector had a dimensionality of 6 (the first-order statistics), 7 (the second-order statistics), and 13 (both order statistics).

To find informative features, the feature importance, method for RFR from the scikit learn package was used, based on finding a partition of the decision tree with the minimum Gini index. To estimate the mean and variance of informative values, predictive models were trained 10 times. As can be seen from Fig. 10(b), the most informative features are the second-order ones – entropy, energy, ASM. However, the high dispersion index indicates the heterogeneity of the obtained results. In Fig. 10(b), the dispersion values are significantly smaller, indicating greater stability of the results obtained. The average value makes the greatest contribution to the information content. In Fig. 10(c) the results are consistent with Fig. 10(b).

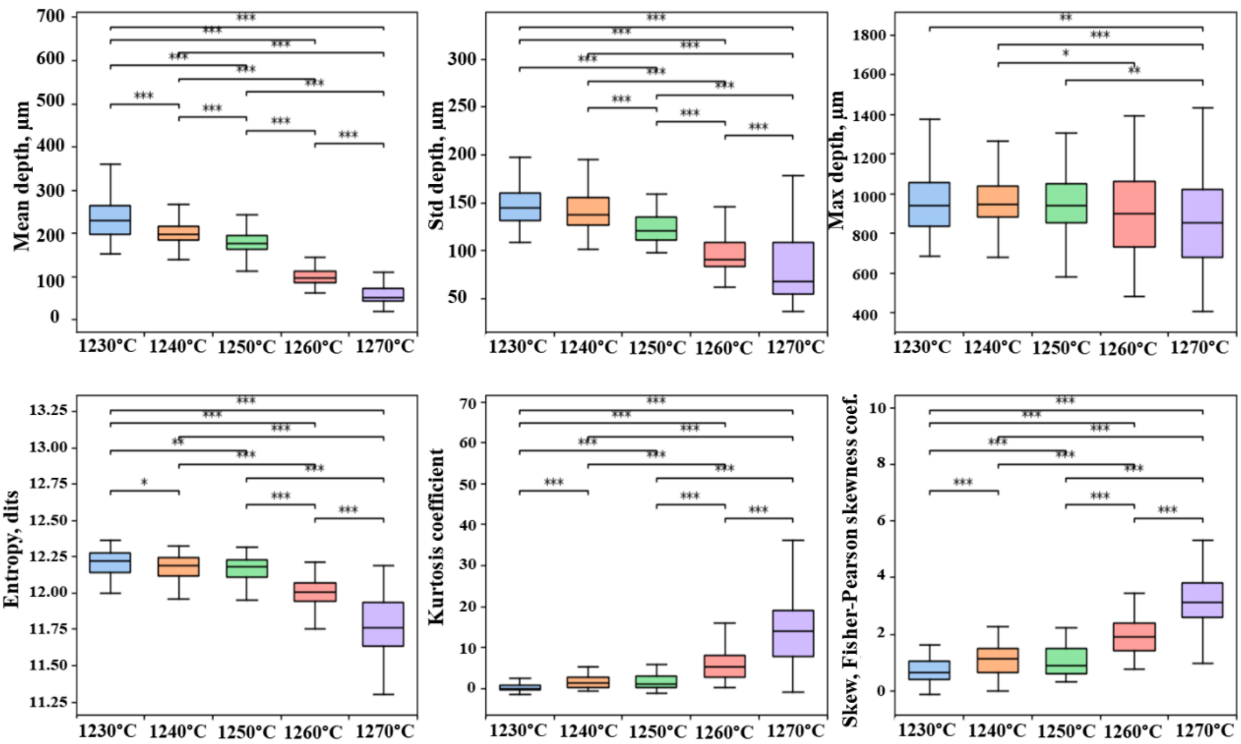

Fig. 7 Distribution of the first order statistics of the depth maps of OCT images. *p<0.05, **p < 0.01, ***p < 0.001 are the significance levels among groups by Mann-Whitney test.

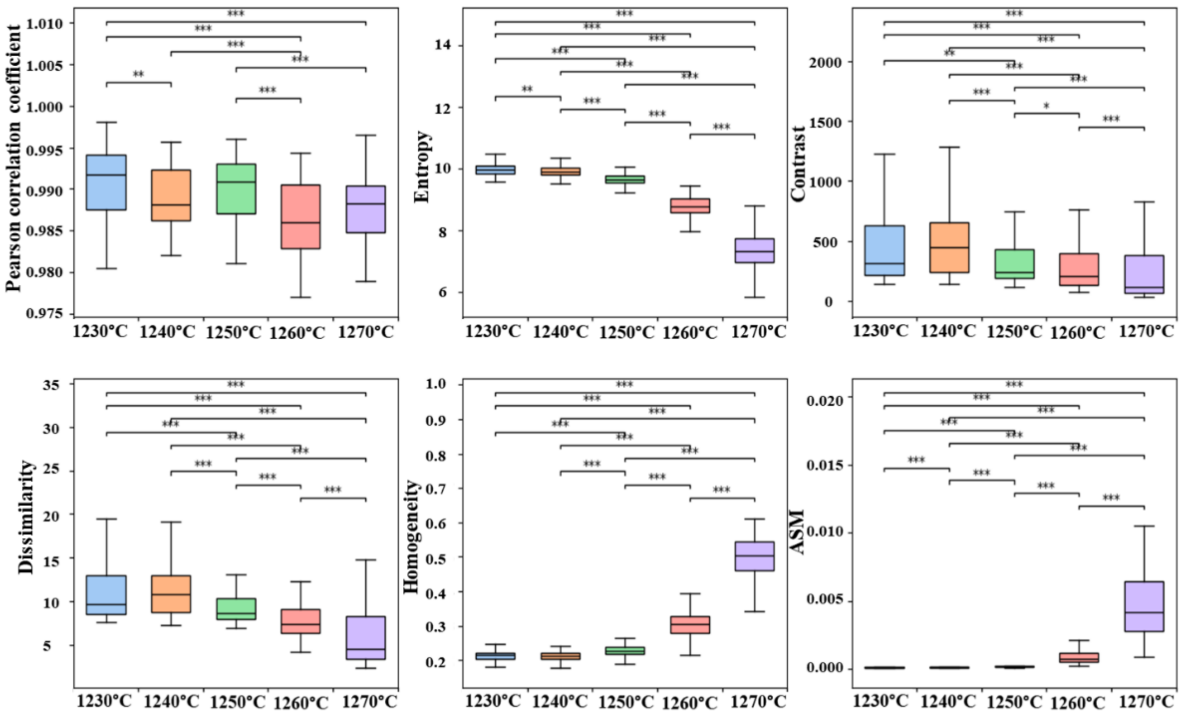

Fig. 8 Distribution of the second order statistics of the depth maps of OCT images. *p<0.05, **p < 0.01, ***p < 0.001 are the significance levels among groups by Mann-Whitney test.

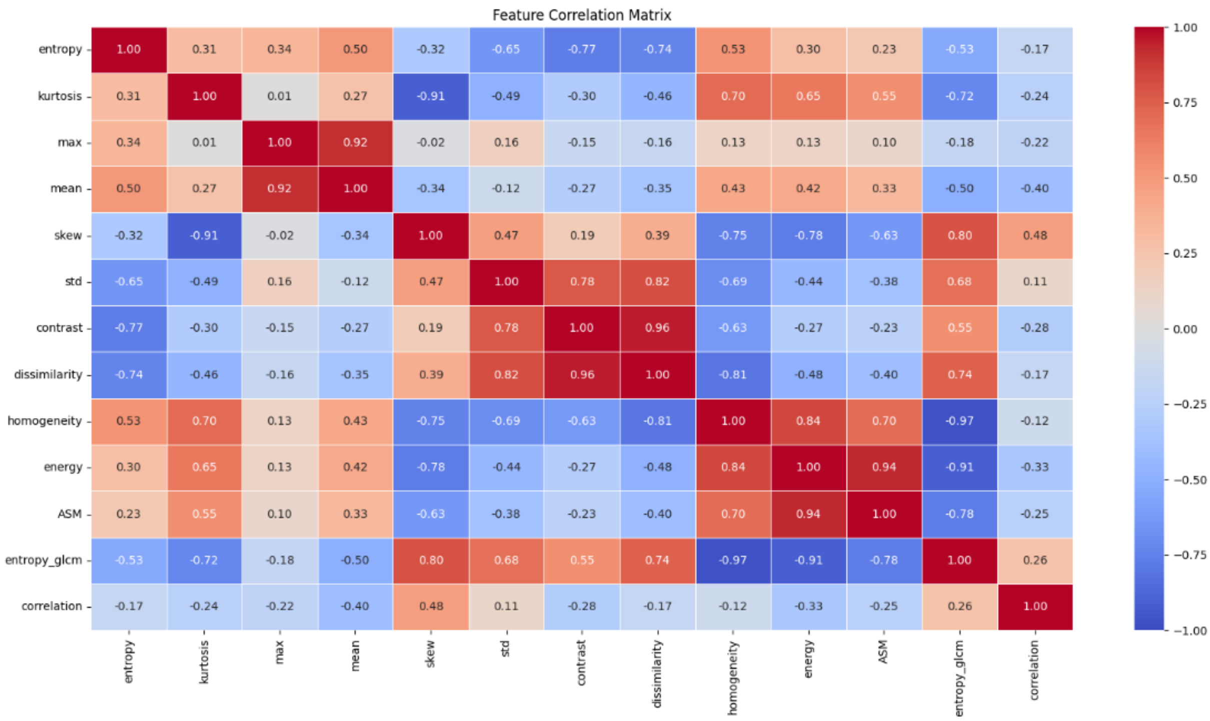

Fig. 9 Correlation matrix for the first and the second order statistics.

Table 1 Accuracy of RFR for the first, the second, and both order statistics.

	First order statistics		**Second order statistics**		**Both**	
	R^2	**MAE (°C)**	R^2	**MAE (°C)**	R^2	**MAE (°C)**
Accuracy (mean ± STD)	0.958 ± 0.046	4.141± 0.651	0.955 ± 0.051	3.671 ± 0.642	0.955 ± 0.052	3.571 ± 0.659

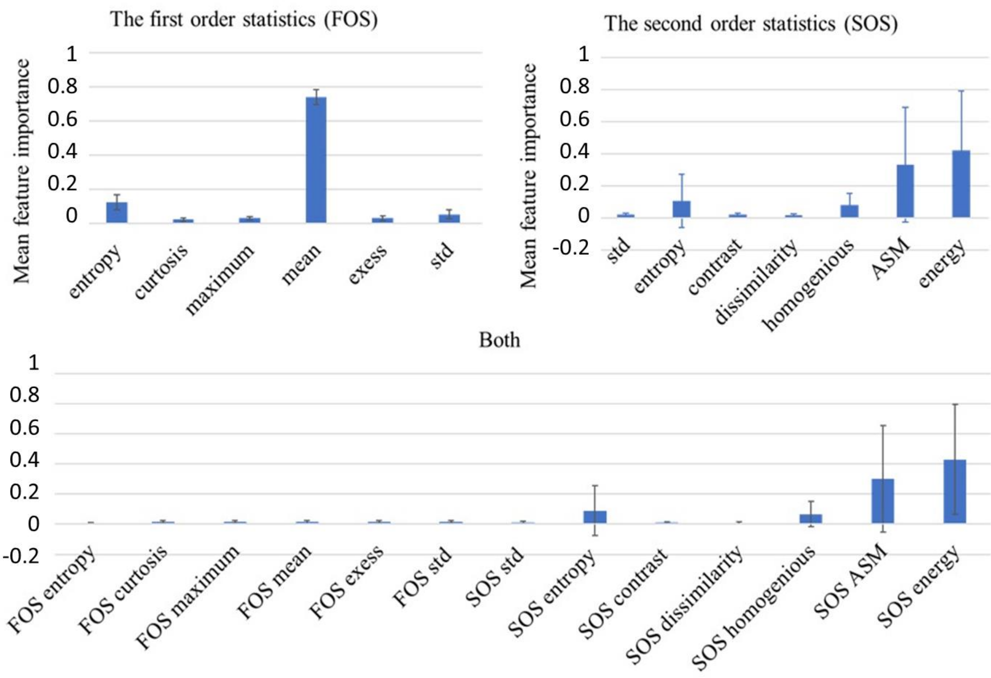

Fig. 10 Feature importance for the first and the second order statistics.

4 Discussion

According to Fig. 7, the mean depth gradually decreases depending on the increase in sintering temperature. Samples with a sintering temperature of 1230 °C have a large average depth, while samples with a sintering temperature of 1270 °C have a minimum average depth. Therefore, it can be assumed that samples with a sintering temperature of 1230 have deeper pores and may be more porous than others. These conclusions can be confirmed by referring to Figs. 5(a) and 5(b), which show that the surface of the sample with a sintering temperature of 1230 °C is more porous than the surface of the sample 1270 °C. It can also be noted that pores maximal depth of all temperature groups is approximately at the same level. However, samples with a sintering temperature of 1270 °C have the lowest maximal depth and statistically significantly differ from almost of other groups. Therefore, by varying the sintering temperature, it is possible to achieve different porosity of the samples, which must be taken into account in manufacturing TiNi implants.

The strengths of the RFR method are the evaluation of complex dependencies (dependence of porosity on sintering temperature, many characteristics required as a result of constructing regression), work on a small amount of data (in our case, 5 groups of 100 images were used), robustness to outliers. Since we propose to describe the depth map with a few key parameters (e.g. average depth, entropy, etc.), RFR data model predicted them better than linear models, which makes it possible to capture complex dependencies without overfitting. RFR offers a compelling trade-off between accuracy and simplicity of sintering temperature-based predictions. While deep learning may outperform it in scenarios with large datasets, the interpretability and low computational cost of RFR makes it well-suited for industrial applications with limited training data. Future work could hybridize RFR with physics-based constraints.

5 Conclusion

The presented results demonstrate that OCT can be used in systems of quality control of porous metal alloy manufacturing. The texture parameters derived from OCT images can be linked to crucial material properties such as porosity, defects (e.g., cracks), and surface or subsurface inhomogeneities. RFR-based approach using OCT depth maps and their the first and the second order statistics was proposed to predict TiNi samples sintering temperature. The RFR model achieves R^2 value of 0.95 for reconstruction of the first- and the second-order OCT image texture metrics. This method provides a robust, interpretable alternative to deep learning approaches for small and medium datasets.

Acknowledgments

The investigation was supported by Russian Science Foundation with the grant № 24-63-00049, https://rscf.ru/en/project/24-63-00049/.

Disclosures

All authors declare that there is no conflict of interest in this paper.

References

1. V. E. Gunter, V. N. Khodorenko, and T. L. Chekalkin, "Medical materials and shape memory implants", Publishing House of MIT, Tomsk (2011). ISBN:9785985890365.
2. J. Zhu, Q. Zeng, and T. Fu, "An updated review on TiNi alloy for biomedical applications," Corrosion Reviews 37(6), 539–552 (2019).
3. W. Cai, Y. F. Zheng, X. Meng, and L. C. Zhao, "Superelasticity in TiNi alloys and its applications in smart systems," Materials Science Forum 475, 1915–1920 (2005).
4. S. H. Mohammed, S. H. Shahatha, "Shape memory alloys, properties and applications: a review," AIP Conference Proceedings, AIP Publishing 2593(1), 020008 (2023).
5. V. Shishkovsky, L. T. Volova, M. V. Kuznetsov, Yu. G. Morozov, and I. P. Parkin, "Porous biocompatible implants and tissue scaffolds synthesized by selective laser sintering from Ti and NiTi," Journal of Materials Chemistry 18(12), 1309–1317 (2008).
6. Z. Wang, Y. Tan, and N. Li, "Powder metallurgy of titanium alloys: a brief review," Journal of Alloys and Compounds 965, 171030 (2023).
7. S. G. Anikeev, N. V. Artyukhova, M. I. Kaftaranova, V. N. Khodorenko, E. V. Yakovlev, A. B. Markov, V. V. Promakhov, and O. R. Mamazakirov, "The influence of electron-beam treatment on the structure of a TiNi powder alloy obtained by calcium-hydride reduction," Journal of Surface Investigation: X-ray, Synchrotron and Neutron Techniques 15, 1067–1071 (2021).
8. N. V. Artyukhova, Yu. F. Yasenchuk, K. Ji-Soon, and V. É. Gunther, "Reaction sintering of porous shape-memory Titanium−Nickelide-based alloys," Russian Physics Journal 57, 1313–1320 (2015).
9. I. A. Drozdov, "Formation of intermetallics in a porous powder Titanium-Nickel diffusion couple," Powder Metallurgy and Metal Ceramics 34(5,6), 62–70 (1995).
10. C. Velmurugan, V. Senthilkumar, and P. S. Kamala, "Microstructure and corrosion behavior of niti shape memory alloys sintered in the SPS process," International Journal of Minerals, Metallurgy, and Materials 26(10), 1311–1321 (2019).
11. T. Miao, S. Zhan, X. Chen, and L. Hu, "Effect of sintering temperature on microstructure characteristics of porous NiTi alloy fabricated via elemental powder sintering," Materials 17(3), 743 (2024).
12. D. Zhao, Y. Yang, J. Liu, G. Yang, Y. Qin, and D. Yin, "Effect of soaking time on the preparation of porous NiTi alloy during fields-activated micro-sintering and forming technology," in 4th International Conference on New Forming Technology (ICNFT 2015), MATEC Web of Conferences 21, 10007 (2015).
13. D. F. Williams, "On the mechanisms of biocompatibility", Biomaterials 29(20), 2941–2953 (2008).
14. N. Viknianshchuk, A. I. Mishanin, S. I. Tverdokhlebov, and A.S. Golovkin, "Approaches to biomaterials testing according to modern biocompatibility paradigm," Translational Medicine 4(1), 29–40 (2017).
15. M. Bahraminasab, B. B. Sahari, "NiTi shape memory alloys, promising materials in orthopedic applications," in Shape Memory Alloys − Processing, Characterization and Applications, F. M. B. Fernandes (Ed.), 262–278 (2013).
16. J. L. Hernandez, K. A. Woodrow, "Medical applications of porous biomaterials: features of porosity and tissue-specific implications for biocompatibility," Advanced Healthcare Materials 11(9), 2102087 (2022).
17. H. J. Haugen, S. Bertoldi, "Characterization of morphology—3D and porous structure," Characterization of Polymeric Biomaterials, 21–53 (2017).
18. Y. Yasenchuk, E. Marchenko, V. Gunther, A. Radkevich, O. Kokorev, S. Gunther, G. Baigonakova, V. Hodorenko, T. Chekalkin, J. Kang, S. Weiss, and A. Obrosov "Biocompatibility and clinical application of porous TiNi alloys made by self-propagating high-temperature synthesis (SHS)," Materials 12(15), 2405 (2019).
19. S. J. Hollister, "Porous scaffold design for tissue engineering," Nature Materials 4(7), 518–524 (2005).
20. F. S. L. Bobbert, A. A. Zadpoor, "Effects of bone substitute architecture and surface properties on cell response, angiogenesis, and structure of new bone," Journal of Materials Chemistry B 5(31), 6175–6192 (2017).
21. C. Torres-Sanchez, F. R. A. Al Mushref, M. Norrito, K. Yendall, Y. Liu, and P. P. Conway, "The effect of pore size and porosity on mechanical properties and biological response of porous titanium scaffolds," Materials Science and Engineering: C 77, 219–228 (2017).
22. Y. Zhang, N. Sun, M. Zhu, Q. Qiu, P. Zhao, C. Zheng, Q. Bai, Q. Zeng, and T. Lu, "The contribution of pore size and porosity of 3D printed porous titanium scaffolds to osteogenesis," Biomaterials Advances 133, 112651 (2022).
23. Q. S. Yan, "Prediction of porosity of porous NiTi alloy from processing parameters based on SVR," Advanced Materials Research 393, 231–235 (2012).
24. V. Maitra, J. Shi, and C. Lu, "Robust prediction and validation of as-built density of Ti-6Al-4V parts manufactured via selective laser melting using a machine learning approach," Journal of Manufacturing Processes 78, 183–201 (2022).
25. T. Kamal, A. Upadhyaya, and Gouthama, "Machine learning based sintered density prediction of bronze processed by powder metallurgy route," Metals and Materials International 29(6), 1761–1774 (2023).
26. L. Mosser, O. Dubrule, and M. J. Blunt, "Reconstruction of three-dimensional porous media using generative adversarial neural networks," Physical Review E 96(4), 043309 (2017).

27. V. V. Nikolaev, T. B. Lepekhina, G. V. Malkin, A. S. Garin, E. S. Marchenko, A. V. Dubrov, M. D. Khomenko, and Y. Kistenev, "Estimating the porosity of Nickel-Titanium (NiTi) implants using optical coherence tomography and machine learning", Journal of Biomedical Photonics & Engineering 10(4), 112–120 (2024).